**PCCP**

# Direct Time-Resolved Detection and Quantification of Key Reactive Intermediates in Diethyl Ether Oxidation at T = 450 – 600 K.

| | |
|---|---|
| Journal: | *Physical Chemistry Chemical Physics* |
| Manuscript ID | CP-ART-07-2020-003861.R1 |
| Article Type: | Paper |
| Date Submitted by the Author: | 26-Sep-2020 |
| Complete List of Authors: | Demireva, Maria; Sandia National Laboratories, Combustion Research Facility<br>Au, Kendrew; Sandia National Laboratories, Combustion Research Facility<br>Sheps, Leonid; Sandia National Laboratories, Combustion Research Facility |
| | |

**SCHOLARONE™**
Manuscripts

# Direct Time-Resolved Detection and Quantification of Key Reactive Intermediates in Diethyl Ether Oxidation at T = 450 – 600 K.

Maria Demireva*, Kendrew Au, and Leonid Sheps*

*Combustion Research Facility, Sandia National Laboratories, Livermore, California 94551, United States*

*Corresponding authors: lsheps@sandia.gov, mdemire@sandia.gov.

**Abstract**

High-pressure multiplexed photoionization mass spectrometry (MPIMS) with tunable vacuum ultraviolet (VUV) ionization radiation from the Lawrence Berkeley Labs Advanced Light Source is used to investigate the oxidation of diethyl ether (DEE). Kinetics and photoionization (PI) spectra are simultaneously measured for the species formed. Several stable products from DEE oxidation are identified and quantified using reference PI cross-sections. In addition, we directly detect and quantify three key chemical intermediates: peroxy (ROO•), hydroperoxyalkyl peroxy (•OOQOOH), and ketohydroperoxide (HOOP=O, KHP). These intermediates undergo dissociative ionization (DI) into smaller fragments, making their identification by mass spectrometry challenging. With the aid of quantum chemical calculations, we identify the DI channels of these key chemical species and quantify their time-resolved concentrations from the overall carbon atom balance at T = 450 K and P = 7500 Torr. This allows the determination of the absolute PI cross-sections of ROO•, •OOQOOH, and KHP into each DI channel directly from experiment. The PI cross-sections in turn enable the quantification of ROO•, •OOQOOH, and KHP from DEE oxidation over a range of experimental conditions that reveal the effects of pressure, $O_2$ concentration, and temperature on the competition among radical decomposition and second $O_2$ addition pathways.

**Introduction**

Oxidation of hydrocarbons and oxygenated organic molecules plays an important role in combustion and atmospheric chemistry.[1, 2] The chemical mechanisms of combustion are complex and involve numerous intermediates, products, and competing reactions that depend on the fuel and on operating conditions, including temperature and pressure. Decades of research have led to detailed insights into these mechanisms, which then enable technological advances. One recent promising technology is the development of low temperature combustion (LTC) engines, where fuel oxidation at reduced temperatures can decrease nitrogen oxide and soot emissions while increasing thermal efficiency.[3-5] A deep understanding of the relevant chemistry at these conditions is necessary for predicting fuel ignition behavior and could help improve engine efficiency through development and use of alternative fuels.

More specifically, compression ignition (CI) engines are controlled to a large extent by low-temperature oxidation. Diethyl ether (DEE) is considered a promising biofuel or additive for CI engines due to favorable characteristics, including a high cetane number (125), low boiling temperature, and low viscosity.[6, 7] Combustion of DEE results in low pollutant emission, and DEE can be prepared by dehydration of ethanol, which can be produced from biological sources.[6, 7] Several experimental studies have explored the high-temperature combustion of DEE.[8-13] In contrast, fewer experiments have studied its low-temperature (below ~1000 K) combustion and measured detailed species profiles that can be useful for model development and validation.[10, 14]

A generalized schematic of oxidation reactions during low-temperature combustion of a hydrocarbon (RH) is shown in Scheme 1.[2, 15] The letters R, Q, and P refer to changes in the molecular core of the fuel during sequential H atom abstractions (i.e., for diethyl ether, $CH_3CH_2OCH_2CH_3$: RH = $C_4H_{10}O$; R = $C_4H_9O$, Q = $C_4H_8O$; P = $C_4H_7O$). H atom removal from

RH forms a radical R•, which reacts with $O_2$ to yield ROO•. This oxygen-centered peroxy radical can decompose back to R• + $O_2$ or eliminate $HO_2$ to produce an alkene. $HO_2$ is unreactive below ~1100 K and this pathway inhibits radical chain branching.[2] ROO• can isomerize via internal H abstraction to yield a carbon-centered hydroperoxyalkyl radical, •QOOH. This transient species plays a key role in determining fuel reactivity by controlling the balance among radical chain propagating and branching channels. Thus far, only two direct kinetics measurements[16, 17] have been obtained for •QOOH reactions, and only one of these studies involved the direct observation of •QOOH.[16] •QOOH can decompose to yield a reactive OH (a chain propagating pathway) or react with a second $O_2$ to form a second peroxy radical, •OOQOOH. Another internal H-shift yields a carbon-centered HOO•POOH radical, which eliminates OH to produce a ketohydroperoxide (KHP, HOOP=O). Decomposition of KHP can yield a second OH and an alkyloxy, •OP=O, such that three reactive radicals are generated for every fuel molecule consumed. The extent of •QOOH decomposition versus reaction with a second $O_2$ impacts fuel ignition properties, and the branching into these and other pathways depends on the fuel structure, temperature, and pressure. Detailed quantitative data on the competition among these channels can serve as critical benchmarks for chemical models, which can aid in the design of emerging fuels and engine technologies.
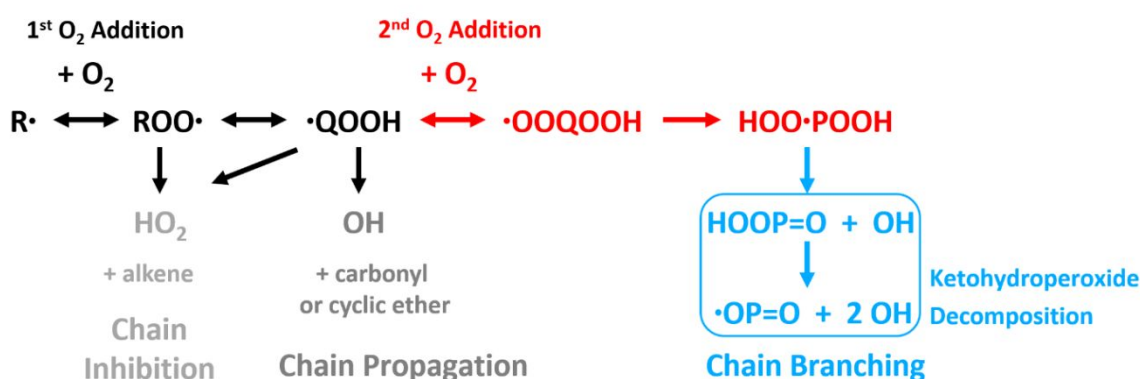


**Scheme 1.** Simplified schematic for the low-temperature oxidation of a hydrocarbon radical, R•.

On a fundamental level, DEE is a prototypical linear ether and a good model system to study the effects of fuel molecular structure (i.e., functional group) on reactivity. Recent results from jet-stirred and plug flow reactors by Tran *et al.*[14] indicated that DEE exhibits two negative temperature coefficient (NTC) zones, in which DEE reactivity decreases with increasing temperature. In the first zone, near 500 K, the reduced reactivity was attributed to an increase in •QOOH thermal decomposition, which diminishes second $O_2$ addition and radical chain branching. In the second NTC region at ~650 K, the decrease in reactivity was explained by the increase in ROO• dissociation back to R• + $O_2$, i.e., the suppression of oxidation altogether. This sensitivity of DEE oxidation to multiple aspects of the underlying reaction sequence makes it a compelling benchmark system for the development of comprehensive sub-mechanisms, provided that key chemical intermediates and products can be measured reliably.

An established technique for investigating complex gas-phase reactions is multiplexed photoionization mass spectrometry (MPIMS) with tunable vacuum ultraviolet (VUV) synchrotron light.[18, 19] This method has demonstrated isomer-specific species quantification from diverse sources including flames, molecular beams, jet-stirred reactors, shock tubes, and photolysis reactors.[18-25] Time-resolved VUV-MPIMS combined with a photolysis flow reactor is particularly powerful for unraveling complex reactions because it reveals the formation and decay timescales of all detected species simultaneously.[24] Photolysis/MPIMS studies have been extensively applied by our group to low-temperature oxidation reactions at low pressures (< 50 Torr).[16, 24, 26-29] Recently, we developed a high-pressure photolysis reactor and coupled it to a highly sensitive MPIMS apparatus,[25] which aided the detection of •OOQOOH and KHP by enhancing second $O_2$ addition pathways.[30-34] However, the key species ROO•, •OOQOOH, and KHP have not previously been quantified experimentally due to the lack of reference PI cross-sections.

Here, we investigate the low-temperature oxidation of DEE at pressures up to 7500 Torr using time-resolved MPIMS and demonstrate a method for quantifying ROO•, •OOQOOH, and KHP directly from experiment. Because these species have unstable or weakly-bound parent cations and fragment upon photoionization, we first identify and assign their dissociative ionization (DI) peaks with the help of theoretical calculations. We then show that at 450 K and 7500 Torr, ROO•, •OOQOOH, and KHP exhibit distinct formation kinetics, which permits their time-dependent absolute concentration profiles to be determined from carbon balancing. Quantification of these species allows for the partial PI cross-sections of their DI fragments to be derived entirely from experiment, which enables the concentrations of ROO•, •OOQOOH, and KHP to be determined at other experimental conditions. From these quantitative data, trends in DEE reactivity can be elucidated as a function of temperature, total pressure, and $O_2$ concentration. Such information will be valuable for developing and improving the accuracy of reaction mechanisms and predictive models for low-temperature hydrocarbon oxidation.

**Methods**

**MPIMS experiments.** The experimental methods and apparatus have been described in detail previously.[24-28, 35] For most of the results presented here, we employed the recently constructed MPIMS with a high-pressure laser photolysis reactor.[25] Dilute flows of DEE and oxalyl chloride (OxCl) in helium were premixed with flows of pure $O_2$ and He in a helical static mixer prior to the reactor. The reactor is 4 cm long with a diameter of 0.5 cm and is lined with quartz inserts to minimize wall reactions. Pulsed 248-nm light from an excimer laser was directed through the reactor to photolyze OxCl[36] and produce Cl atoms that initiate the oxidation of DEE by H abstraction. Studies were carried out at constant temperature (400 – 600 K) and pressure

(1500 − 7500 Torr). A list of experimental conditions is provided in Table S1. The gas flow velocity was chosen to replace the sample mixture between photolysis pulses (typically at 4 Hz). A small central portion of the gas exited the reactor through a pinhole, expanding into a vacuum chamber, and was intersected by tunable VUV ionizing radiation from a monochromator-equipped terminal of the Chemical Dynamics Beamline 9.0.2 at the Lawrence Berkeley Advanced Light Source. VUV energies were typically scanned in the 8.5 − 11 eV range using 0.025 eV steps, and photon flux was measured by an SXUV-100 photodiode. Photoions traveled through electrostatic focusing optics to reach an orthogonal acceleration region, where these ions were subsequently pulsed and detected with a reflectron time-of-flight (TOF) mass spectrometer. A TOF repetition rate of 40 kHz was used, producing a complete mass spectrum every 25 μs over a 250 ms time range (as determined by the photolysis laser repetition rate). The photolysis laser was triggered after 30 ms, giving an experimental time window of $t$ = -30 to 220 ms relative to the photolysis pulse (at $t$ = 0), which started the Cl-initiated oxidation of DEE.

Scanning the VUV photon energy results in a three-dimensional data set, where ion intensity is measured as a function of $m/z$, photon energy, and time.[24] Figure 1 shows a typical photon energy- and time-integrated ($E$ = 8.5 − 11 eV, $t$ = 0 − 30 ms) mass spectrum of Cl-initiated low-temperature DEE oxidation at P = 1500 Torr and T = 500 K. The mass spectrum has been background subtracted for pre-photolysis signal and reveals the depletion of DEE and the formation of products. Insets in Figure 1 show representative time-integrated PI spectra and energy-integrated time traces for the product ion at $m/z$ 44 (acetaldehyde) and the depletion of $m/z$ 74 (DEE).
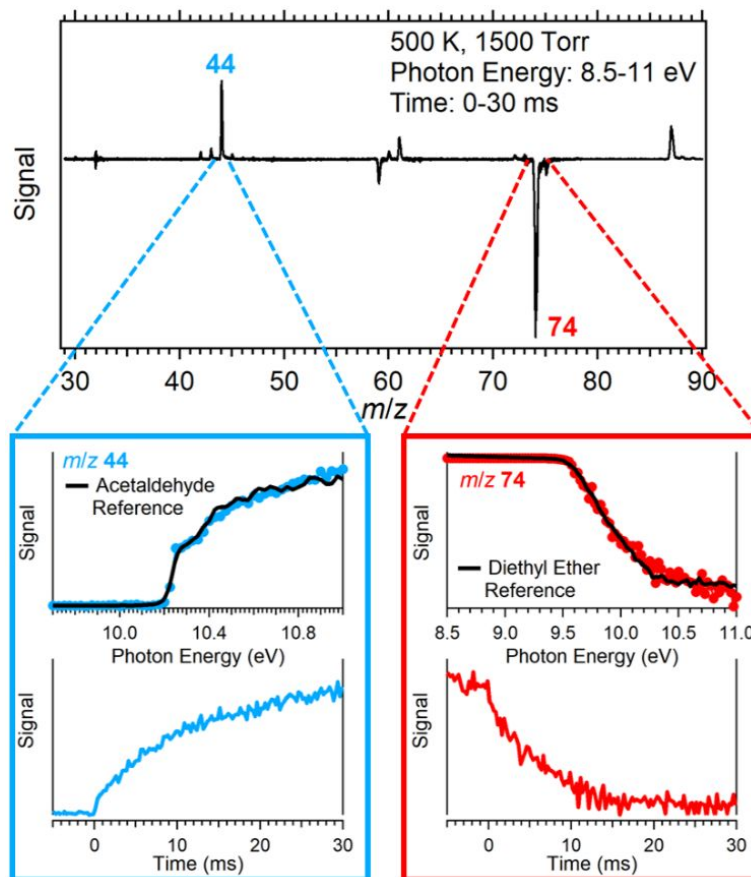
**Figure 1.** A representative background-subtracted photon energy and time-integrated mass spectrum from Cl-initiated DEE oxidation at P = 1500 Torr and T = 500 K. The insets show time-integrated PI spectra and energy-integrated time traces for the product at $m/z$ 44 (acetaldehyde) and for the depleted DEE ($m/z$ 74).

As described previously,[35] species with known PI cross-sections can be quantified from the MPIMS ion signals. The measured ion signals in our experiments are affected by mass-dependent detection bias, which changes with experimental conditions. Thus, prior to each experiment, a calibration mixture containing species with known PI cross-sections that span the relevant $m/z$ range (1% $CH_4$, 0.5% Ar, 0.1% Kr, and 0.1% Xe diluted in He) was used to determine mass discrimination factors (MDFs), which were applied to correct the observed ion intensities. The time-integrated concentration ($N_x$), in the experimental time range (typically 0-30 ms), for species $x$ was then determined using its PI spectrum (integrated over this time range and corrected for the MDF and VUV photon flux) and equation (1):

$$N_x = \left(\frac{\sigma_{DEE}(E)}{S_{DEE}(E)}\right)\left(\frac{S_x(E)}{\sigma_x(E)}\right)N_{DEE} \tag{1}$$

Here, $S_{DEE}(E)$ is the time-integrated, MDF corrected pre-photolysis PI spectrum of DEE, $\sigma_{DEE}(E)$ is the reference PI cross-section of DEE, $S_x(E)$ is the time-integrated, MDF corrected PI spectrum for species $x$, $\sigma_x(E)$ is the reference PI cross-section of $x$, and $N_{DEE}$ is the known time-integrated pre-photolysis concentration of DEE. To obtain the concentration profile for species $x$, its time-dependent signal was scaled such that the time-integrated concentration was equal to $N_x$.

**Theoretical calculations.** Quantum chemical calculations were performed with Gaussian16,[37] using the composite CBS-QB3 method.[38] Adiabatic ionization energies (AIEs) were determined from the energy difference of optimized neutral and cationic structures. For species with unbound cations (ROO• and •OOQOOH), vertical ionization energies (VIEs) were also calculated, in which the energy of the cation was determined at the optimized geometry of the neutral species. Additional calculations were carried out to map out the energy minima and saddle points for dissociation channels on the cation potential energy surfaces (PESs). The results of these calculations were compared to the observed ion signal onsets, aiding in the assignment of DI fragments in the mass spectra.

**Results and Discussion**

**Identification and quantification of products from references.** As part of this work, we measured reference PI spectra for acetaldehyde, diethyl ether, ethyl vinyl ether, 2-methyl-1,3-dioxolane, and acetic anhydride, as detailed in the Supplementary Information. These measurements are in good agreement with the literature cross-sections for acetaldehyde[39] and diethyl ether,[40] and we use our own reference cross-sections when possible to minimize systematic errors in species quantification. A typical mass spectrum, integrated over kinetic time $t = 0 - 30$

ms and photon energy 8.5 – 11 eV at 450 K and 7500 Torr, is shown in Figure 2. The pre-photolysis

ion signals were subtracted, which results in negative signal for DEE at the mass of its parent ion,

$m/z$ 74, and DI fragments at $m/z$ 73 and 59. The time trace as well as the observed PI spectrum for

the depleted DEE signal along with the reference spectrum are shown in Figure S6. To focus on

the products, the negative signals from DEE consumption are not shown in Figure 2.
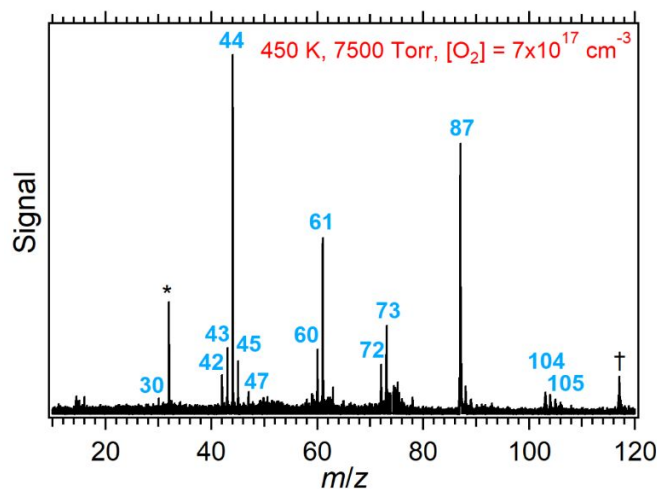


**Figure 2.** Photon energy (8.5-11 eV) and time (0-30 ms) integrated mass spectrum from Cl-initiated oxidation of DEE at 450 K, 7500 Torr, and $[O_2] = 7 \times 10^{17}$ cm$^{-3}$. Peaks arising from species formed in DEE oxidation are labeled by their $m/z$. The depleted ion peaks arising from DEE are not shown. The asterisk marks the $O_2^+$ peak that results from trace amount of residual higher-energy VUV radiation ionizing $O_2$, which is present in large concentration in our experiments. The dagger marks a spurious photolysis-induced artifact at $m/z$ 117, which does not affect the measurements of other peaks.

There are 13 transient mass peaks in Figure 2 that are due to chemical species, formed in

DEE oxidation. Of these, six peaks can be unambiguously assigned to stable products by

comparison with reference PI spectra, as shown in Figure S7: formaldehyde, $m/z$ 30;[41] ketene, $m/z$

42;[42] acetaldehyde, $m/z$ 44; methyl peroxy, $m/z$ 47;[43] acetic acid, $m/z$ 60;[44] and ethyl vinyl ether,

$m/z$ 72. From fits to the reference spectra, these six products were quantified using equation (1)

and their time-dependent concentration profiles are given in Figure S8. Acetaldehyde and ethyl

vinyl ether exhibit short rise times, consistent with primary products of the first $O_2$ addition.

Ketene, methyl peroxy, and acetic acid display slower signal growth and likely arise from

subsequent reactions. The kinetics of formaldehyde are difficult to classify due to large statistical noise; however, $CH_2O$ is a minor product.

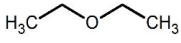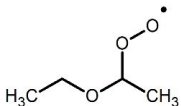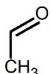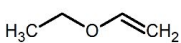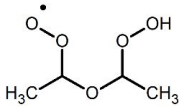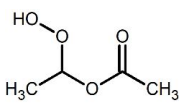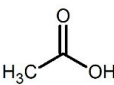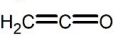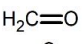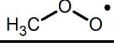The remaining 7 transient mass peaks at $m/z = 43, 45, 61, 73, 87, 104$, and 105 do not match any available reference PI spectra, and their detailed analysis is presented below. The ion peak assignments of all observed stable products and reaction intermediates are summarized in Table 1.

**Isomer distributions in the low-temperature oxidation of DEE.** A schematic of the major reaction pathways in our experiments, based on reported reaction mechanism of Tran *et al.*[14] and theoretical calculations by Sakai *et al.*[45, 46] and Danilack *et al.*,[47] is shown in Scheme 2. H abstraction occurs at the α or β carbon of DEE with calculated C-H bond energies of ~95 and ~102 kcal·mol^{-1}, respectively.[14, 45] In our experiments, H abstraction is initiated by Cl atoms to yield HCl, which has a bond energy of 102.4 kcal·mol^{-1}.[48] Thus, α-R• (1-ethoxyethyl) formation is exothermic by ~7 kcal·mol^{-1}, whereas β-R• (2-ethoxyethyl) formation is thermoneutral. Although the precise α-R•/β-R• ratio cannot be determined solely from the bond energy difference, we expect α-R• to dominate in our experiments. In realistic autoignition devices H abstraction is mainly by OH, rather than by Cl atoms. Yet, even in this case, Tran *et al*. found that α-R• accounts for 94% of all initial radicals at 500 K.[14] To check the assumption that α-R• is the dominant isomer at our conditions, we performed additional experiments at P = 7500 Torr and T = 500 – 600 K.
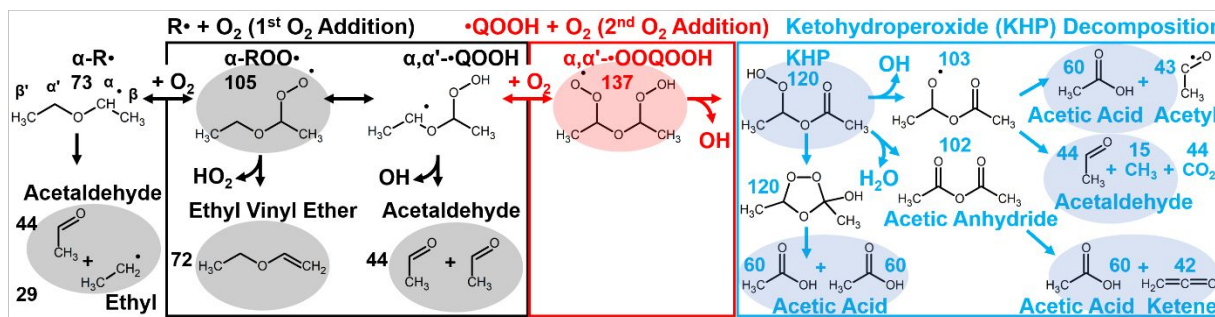


**Scheme 2.** The main pathways for decomposition and oxidation of the 1-ethoxyethyl radical (α-R•, 73 Da), which is the dominant DEE radical formed in our Cl-initiated oxidation experiments. The mass for each species is given in bold and the species observed in our experiments are shaded.

**Table 1.** Chemical species identified from Cl-initiated oxidation of diethyl ether at 450 K and 7500 Torr.

| Species | | $m/z$ | Ion | Co-Fragment |
|---|---|---|---|---|
| Diethyl Ether | $H_3C\diagup O \diagdown CH_3$ | 74[a] | $C_4H_{10}O^+$ | |
| | | 73[a, b] | $C_4H_9O^+$ | H |
| | | 59[a, b] | $C_3H_7O^+$ | $CH_3$ |
| *1st O$_2$ Addition* | | | | |
| ROO• (105 Da) | | 73[b, c] | $C_4H_9O^+$ | $O_2$ |
| | | 45[b, d] | $C_2H_5O^+$ | $O_2, C_2H_4$ |
| Acetaldehyde | | 44[a] | $C_2H_4O^+$ | |
| | | 43[c] | $C_2H_3O^+$ | H |
| Ethyl Vinyl Ether | $H_3C\diagup O \diagdown CH_2$ | 72[c] | $C_4H_8O^+$ | |
| | | 44[b, c] | $C_2H_4O^+$ | $C_2H_4$ |
| | | 43[b, c] | $C_2H_3O^+$ | $C_2H_5$ |
| *2nd O$_2$ Addition* | | | | |
| •OOQOOH (137 Da) | | 105[b, c] | $C_4H_9O_3^+$ | $O_2$ |
| | | 104[b, d] | $C_4H_8O_3^+$ | $HO_2$ |
| | | 61[b, c] | $C_2H_5O_2^+$ | $O_2, C_2H_4O$ |
| | | 45[b, d] | $C_2H_5O^+$ | $O_2, C_2H_4O_2$ |
| Ketohydroperoxide (KHP) | | 120[c] | $C_4H_8O_4^+$ | |
| | | 87[b, c] | $C_4H_7O_2^+$ | $HO_2$ |
| | | 61[b, c] | $C_2H_5O_2^+$ | $CH_3, CO_2$ |
| | | 43[b, d] | $C_2H_3O^+$ | $HO_2, C_2H_4O$ |
| Acetic Acid | | 60[a] | $C_2H_4O_2^+$ | |
| Ketene | $H_2C{=}C{=}O$ | 42[a] | $C_2H_2O^+$ | |
| Formaldehyde | $H_2C{=}O$ | 30[a] | $CH_2O^+$ | |
| Methyl Peroxy | | 47[a] | $CH_3O_2^+$ | |

[a] PI cross-section known from literature.   [b] Dissociative ionization fragment.   [c] PI cross-section determined in this work.   [d] PI cross-section is unknown.

The key results of these temperature-dependent experiments are shown in Figure 3, which compares the concentration of DEE consumed to the total concentration of quantified products from reference PI spectra. The time traces in Figure 3 have been carbon-weighted by scaling the concentration profiles by the number of carbon atoms (e.g., DEE consumption scaled by 4, acetaldehyde scaled by 2). Figure 3 indicates that acetaldehyde is the main quantified product at all temperatures, accounting for 86% of all quantified products at 600 K.
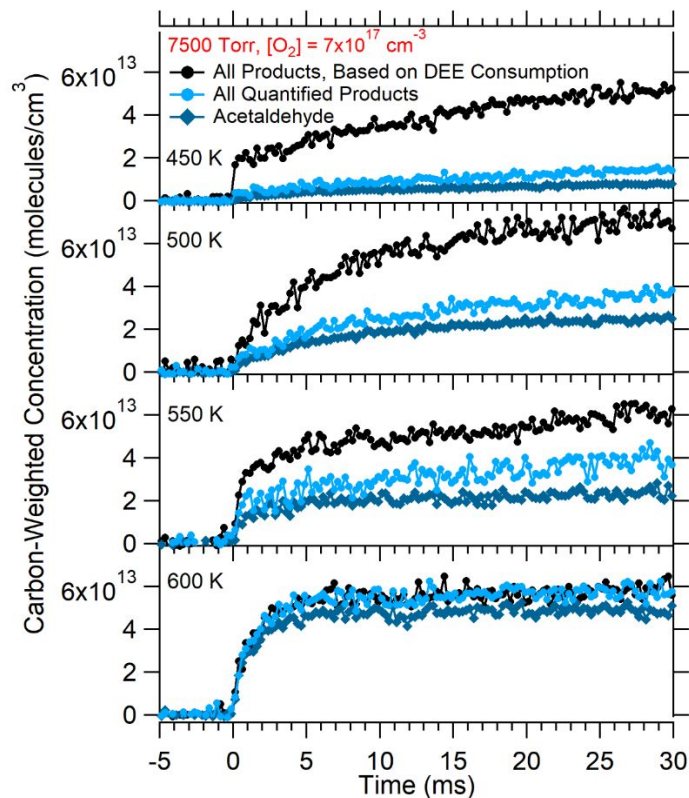
**Figure 3.** Total carbon-weighted concentration of all products, quantified via reference PI spectra (blue circles), compared with that expected from DEE consumption (black circles) as a function of temperature at P = 7500 Torr. The carbon-weighted concentration of acetaldehyde (diamonds) is included for comparison.

Based on the low-temperature DEE oxidation pathways reported by Tran *et al.*[14] and Sakai *at al.*,[45] acetaldehyde forms solely *via* decomposition and oxidation channels of α-R•. Specifically, Sakai *et al.* performed quantum chemical calculations of the β-R• + $O_2$ PES and found that there are no energetically accessible pathways from β-ROO• to acetaldehyde. In addition, $CH_3CHO$ is not likely to be produced by secondary chemistry in our experiments under high-$O_2$ conditions, because our initial radical concentrations are low and most reactive radicals react rapidly with $O_2$. Thus, the results in Figure 3 confirm that at least 86% of DEE radicals formed in our experiments at 600 K are α-R• radicals. The other species, quantified at 600 K in Figure 3, are $CH_2O$ (7%), acetic acid (4%), ethyl vinyl ether (2%), and $CH_3OO•$ (1%). These species can also form from

α-R•, thus, the proportion of this initial radical isomer is likely higher than 86% at 600 K.

Another argument in favor of the dominance of α-R• comes from our earlier study on the Cl-initiated oxidation of tetrahydrofuran (THF), in which we demonstrated that the α-R• isomer accounted for > 96% of the initial radicals at 600 K.[31] The selectivity of Cl-initiated abstraction should be even greater below 600 K. Notably, the $C_\alpha$-H bond energy in THF is only 4.5 kcal·mol$^{-1}$ lower than the $C_\beta$-H bond energy,[49] compared to 7.5 kcal·mol$^{-1}$ in DEE. Considering our THF results (96% α-R• at 600K), the result of Tran *et al.* (94% α-R• at 500 K from OH-initiated DEE oxidation) and our present results from Figure 3, we estimate that the contribution of β-R• in our experiments is << 4%.

As shown in Scheme 2, α-R• can decompose to form acetaldehyde and ethyl radical, and indeed we detected both of these products in supporting experiments, performed at 7300 Torr and 500 K in the absence of $O_2$. In the presence of oxygen, α-R• reacts with $O_2$ to produce α-ROO•. Elimination of $HO_2$ from α-ROO• yields ethyl vinyl ether, which we observe at *m/z* 72. At 450 K and 7500 Torr, the concentration of ethyl vinyl ether is about a factor of 10 smaller than that of acetaldehyde (see Figure S8) indicating that the $HO_2$ elimination channel plays a minor role. Alternatively, α-ROO• can undergo intramolecular H atom migration to form •QOOH. There are three possible isomers of •QOOH, depending on the carbon (α', β, or β', see Scheme 2) from which H transfers, and isomerization to α,α'-•QOOH is strongly favored due to the weaker C-H bond at the α' site. Calculations by Sakai *et al.* indicate that at 500 K and in the high pressure limit the α,α'-•QOOH isomer dominates over the other two isomers by at least a factor of ~1000 and that the lowest energy channel for OH elimination from α,α'-•QOOH is β-scission, which produces two acetaldehyde molecules + OH.[45] The high yield of acetaldehyde, especially with increased temperature, observed in our experiments (Figure 3) is consistent with this β-scission pathway.

Because acetaldehyde is not produced from the other two •QOOH isomers, this high yield of acetaldehyde provides experimental evidence that isomerization of α-ROO• leads predominantly to the α,α'-•QOOH isomer at our conditions.

A second $O_2$ molecule can react with α,α'-•QOOH to form α,α'-•OOQOOH. The second $O_2$ addition competes with β-scission of α,α'-•QOOH and plays an important role in determining the reactivity of DEE. Isomerization of α,α'-•OOQOOH *via* another H atom transfer from the α carbon results in the immediate elimination of OH and formation of α,α'-KHP.[47] In the following discussion, we consider only the dominant isomers of the key intermediates and omit the α/α' atom labels for brevity, referring to them simply as R•, ROO•, •QOOH, •OOQOOH, and KHP. There are several possible decomposition pathways for KHP as proposed in Scheme 2 that affect DEE reactivity differently. For example, O-OH bond scission is a radical chain branching pathway that produces a second OH and an alkyloxy radical, contributing three radicals for every fuel molecule consumed. The alkyloxy can undergo β-scission to form acetaldehyde + $CH_3CO_2$ (likely decomposing into $CH_3$ and $CO_2$) or undergo internal H atom transfer to generate acetic acid and acetyl. The latter process should be favored because calculations indicate that the barrier and asymptotic product energy for this channel are lower than those for the acetaldehyde + $CH_3CO_2$ pathway.[47] The other KHP decomposition channels shown in Scheme 2 lead to closed-shell products and are thus chain propagating, i.e. one reactive OH radical is co-produced with KHP for every fuel molecule consumed. Specifically, KHP decomposition *via* a Korcek mechanism can produce two unreactive acetic acid molecules, and $H_2O$ elimination from KHP yields acetic anhydride, which can subsequently dissociate to form acetic acid + ketene. Determining the branching of KHP into reactive vs. unreactive pathways is important for understanding DEE reactivity. In our experiments, both acetic acid (*m/z* 60) and ketene (*m/z* 42) are produced with

15

longer rise times than acetaldehyde, which is consistent with the time behavior expected for products from the second $O_2$ addition. Although we can quantify all products of KHP decomposition, discerning the contribution of each pathway is complicated by acetic acid being able to form *via* all three pathways. A determination of the branching into the various KHP decomposition channels, supported by kinetics modeling, will be reported in a future publication.

**Identification of ROO•, •OOQOOH, and KHP.** Figure 3 shows that at 450 K and 7500 Torr, only ~25% of the carbon atom balance can be quantified using reference PI spectra. The major intermediates expected to be present but not yet identified are ROO• (105 Da), •OOQOOH (137 Da), and KHP (120 Da). •QOOH is almost certainly very short-lived and occurs in vanishingly small mole fraction. To assess the contributions of ROO•, •OOQOOH, and KHP to the observed ion signals, we now consider the unassigned peaks at $m/z$ = 43, 45, 61, 73, 87, 104, and 105, whose masses indicate that most (or all) of them are daughter ions from larger species that fragment upon photoionization.

To aid with DI peak assignments we performed calculations using the CBS-QB3 method. Cation PESs for the dominant ROO•, •OOQOOH, and KHP isomers are shown in Figure S9, and a summary of possible DI channels is given in Figure 4. For simplicity, we consider only two KHP conformers: the lowest-energy conformer (with an internal H bond, similar to the lowest-energy KHP conformer of dimethyl ether, DME),[50] and a conformer without the H bond (which is 0.19 eV higher in energy). For ROO• and •OOQOOH, we consider a single conformer; a full conformational search for these intermediates is outside the scope of this paper. We summarize the ion peak assignments below and provide full details in the Supplementary Information.

Our calculations indicate that ROO and OOQOOH cations are unbound, with VIEs of 9.98 eV and 10.07 eV, respectively, to form $ROO^+$ and $OOQOOH^+$ in the triplet ground electronic state.
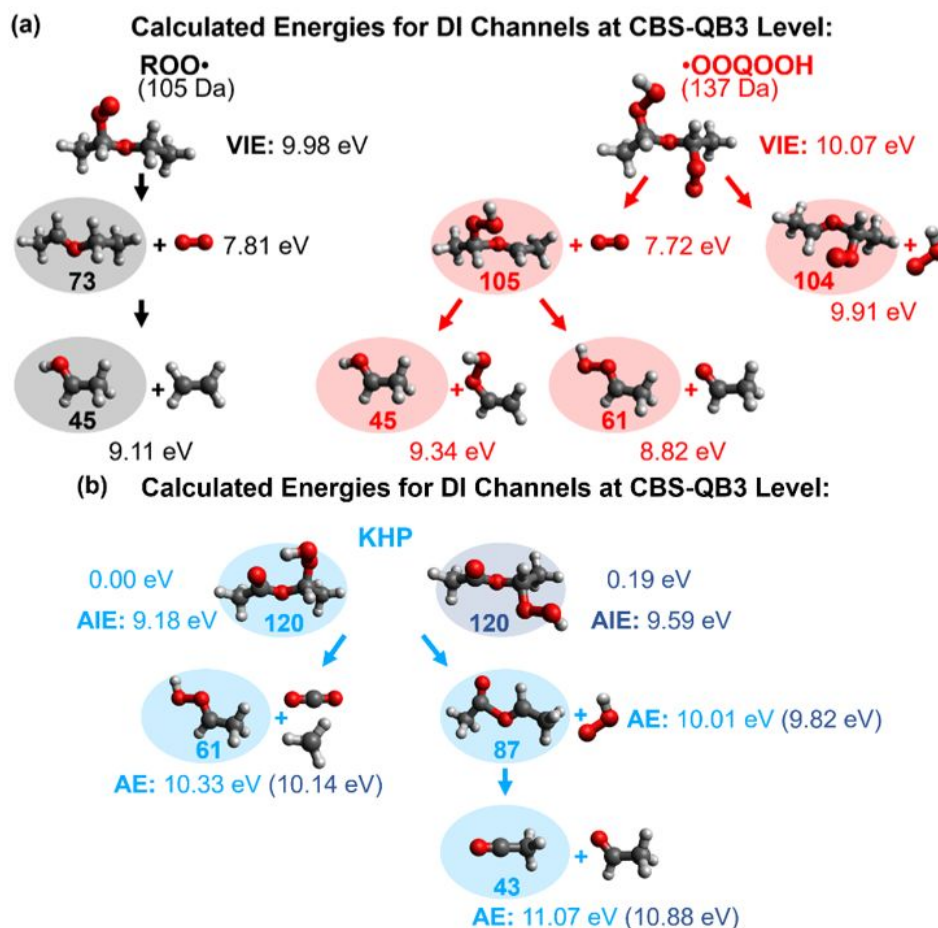
**Figure 4.** Major DI channels identified for (a) ROO• and •OOQOOH, and (b) KHP in our DEE oxidation experiments. Calculations indicate that the cations of ROO•, and •OOQOOH are unbound whereas the cations of the two KHP conformers considered here are bound. The detected ions are labeled with shaded ovals and their corresponding *m/z* is given in bold. Energies are referenced to the neutral species; VIE, AE, and AIE refer to vertical ionization, appearance, and adiabatic ionization energy, respectively.

Following photoionization, ROO$^+$ completely dissociates via barrierless O$_2$ elimination to form R$^+$ at *m/z* 73 (7.81 eV above neutral ROO•), which can dissociate further into CH$_3$CHOH$^+$ (*m/z* 45) + CH$_2$CH$_2$ (9.11 eV above ROO•). OOQOOH$^+$ decomposes to QOOH$^+$ (*m/z* 105) + O$_2$ at 7.72 eV above •OOQOOH; QOOH$^+$ can further fragment into CH$_3$CHOOH$^+$ (*m/z* 61) + CH$_3$CHO (8.82 eV). All these DI pathways lie below the VIEs of the parent cations, and therefore we expect the onsets of these fragment ions to be near the VIEs to form ROO$^+$ and OOQOOH$^+$, at ~10 eV. In addition, decomposition of OOQOOH$^+$ into OOQ$^+$ (*m/z* 104) + HO$_2$ and QOOH$^+$ into CH$_3$CHOH$^+$ (*m/z* 45) + CH$_2$CHOOH are energetically feasible at 9.91 and 9.34 eV above

17

•OOQOOH; however, we could not optimize transition states for the latter DI channel and consider it tentative.

The KHP conformers that we considered have bound parent cations with AIEs of 9.18 and 9.59 eV. Both cation conformers can eliminate $HO_2$ without a barrier to form $CH_3C(O)OCHCH_3^+$ (*m/z* 87) with asymptotic energy of 10.01 eV relative to the lowest-energy neutral conformer. The *m/z* 87 DI fragment can further decompose into $CH_3CO^+$ (*m/z* 43) + $CH_3CHO$ at an asymptotic energy of 11.07 eV. The KHP parent cations can also eliminate $CH_3$ *via* a barrier of 10.33 eV to yield a weakly-bound $CH_3CHOOH^+ \cdot CO_2$ adduct (*m/z* 105), which should rapidly eliminate $CO_2$ in a barrierless process to form $CH_3CHOOH^+$ (*m/z* 61) + $CO_2$ + $CH_3$ at an asymptotic energy of 10.15 eV. The time trace of the *m/z* 105 peak, as shown below (Figure 5), exhibits no evidence of contribution from KHP, confirming that this pathway produces only *m/z* 61 ions. This pathway is analogous to the $CH_3CO^+$ (*m/z* 43) + $CH_3$ + $CO_2$ DI channel of the acetic anhydride cation.[51] The asymptotic energies and barriers for the DI channels of KHP are higher than the AIE and thus correspond to the expected appearance energies of these fragment ions in our experiments. If the higher-energy KHP conformer is ionized, the appearance energies will be reduced by 0.19 eV.

The calculated cation PESs suggest that each DI peak at *m/z* 73, 105, and 87 arises from a single species: ROO•, •OOQOOH, and KHP, respectively. The time traces for these peaks, scaled for visual comparison, are shown in Figure 5. The *m/z* 73 signal has been corrected for a negative contribution (depletion) due to a DI fragment of DEE, using the partial PI cross-section of DEE into the *m/z* 73 channel, as illustrated in Figure S10. The *m/z* 73 ions are produced immediately after the photolysis pulse, whereas formation of *m/z* 105 and 87 ions is progressively slower. This trend is consistent with the expected sequence of rise times of ROO•, •OOQOOH, and KHP, respectively, supporting the peak assignments from computations.

Physical Chemistry Chemical Physics
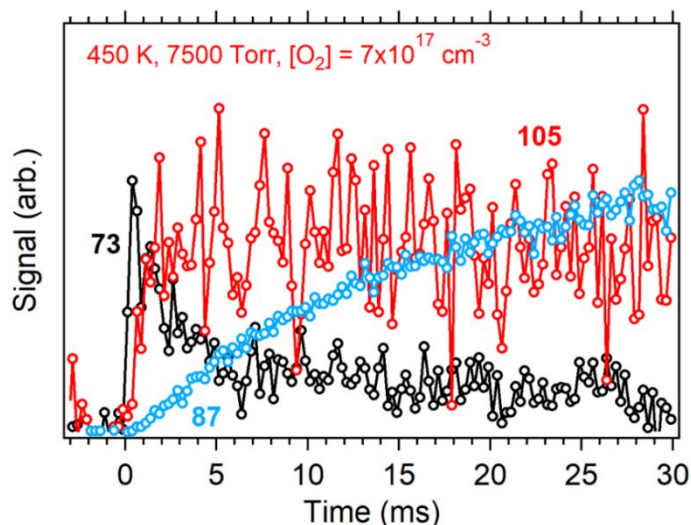


**Figure 5.** Time-dependent signals (integrated over 8.5-11 eV) for ions at *m/z* 73, 105, and 87 (scaled for visual comparison) at 450 K and 7500 Torr. The signal for the *m/z* 73 ion has been corrected for the interference from the DI of DEE.

The remaining unassigned ion peaks may contain contributions from the DI of multiple species, which we deconvolve using the time behavior of ROO•, •OOQOOH, and KHP, as determined by the unique DI peaks at *m/z* 73, 105, and 87. A key point in our analysis is that DI occurs in the MPIMS apparatus after sampling from the reactor, so that all fragment ions from a given species exhibit the time evolution of the parent compound. The time trace of an ion peak containing DI signals from multiple species is the sum of the time traces of the contributing species, weighted by their respective PI cross-sections. For example, according to the calculations, the intense *m/z* 61 mass peak arises from the DI of •OOQOOH and KHP. The time-dependent signal for this peak can be fit very well to a weighted sum of the •OOQOOH (*m/z* 105) and KHP (*m/z* 87) time traces as shown in Figure 6(a). The time-integrated (0-30 ms) PI spectrum can also be deconvolved to give the individual PI spectra for the DI of •OOQOOH and KHP into the *m/z* 61 channels. Because •OOQOOH is formed faster than KHP and dominates the signal for the first 3 ms, the PI spectrum for the DI fragment of •OOQOOH can be derived by integrating over the initial 3 ms and scaling proportionally to obtain the expected signal from integration over the entire

30 ms range. The KHP contribution is then obtained from the remaining PI spectrum at *m/z* 61, as shown in Figure 6(b). As described in the Supplementary Information, we use a similar deconvolution procedure to deduce possible DI contributions from ROO•, •OOQOOH, and KHP to the time traces of the remaining unassigned mass peaks at *m/z* 45, 43, and 104. The results from the time trace analysis are fully consistent with the pathways in Figure 4, and DI peak assignments are included in Table 1.
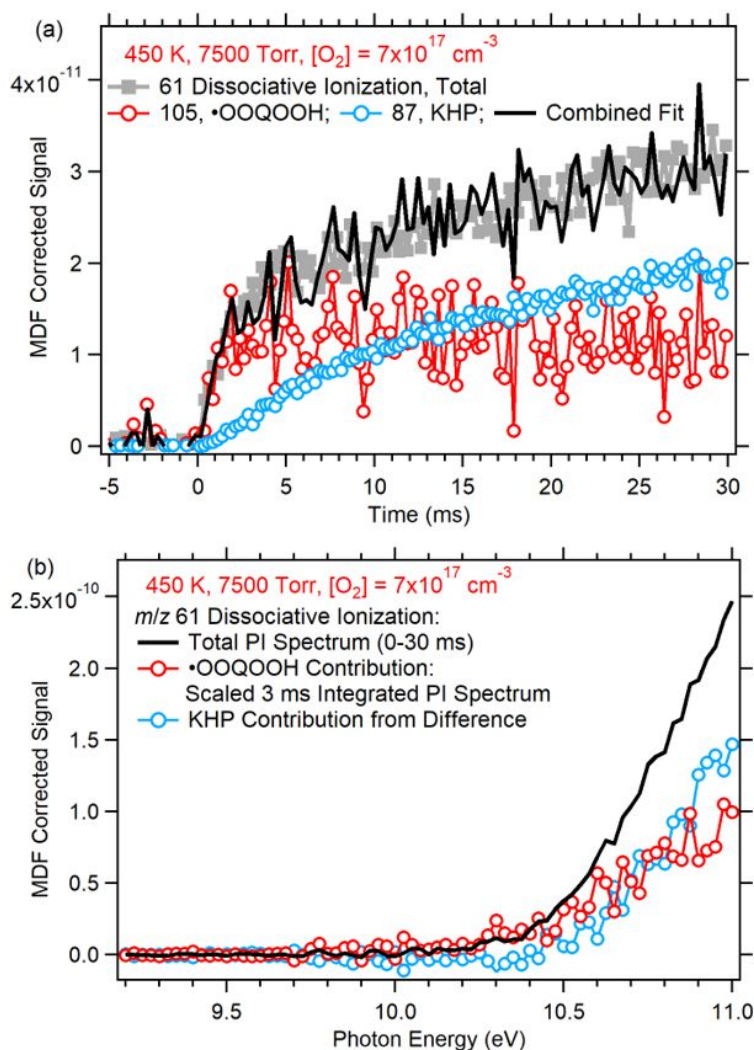


**Figure 6**. (a) Fit (line) of the total *m/z* 61 time trace (integrated over 8.5-11 eV, gray) to a weighted sum of the time traces of •OOQOOH (from *m/z* 105, red) and KHP (from *m/z* 87, blue). (b) Deconvolving the time-integrated (0-30 ms) PI spectrum of *m/z* 61 into the contributions from •OOQOOH (from scaled PI spectrum at *t* = 0 − 3 ms) and KHP (remainder). For details, see text.

**Quantification of ROO•, •OOQOOH, and KHP.** As discussed above, all significant

mass peaks in Figure 2 can be assigned to either stable DEE oxidation products or the reactive

intermediates ROO•, •OOQOOH, and KHP. Figure 3 shows that the mole fraction of these

intermediates (which cannot be quantified using reference PI spectra) is ~0.75 at 450 K and 7500

Torr. The time-dependent total concentration of these intermediates can be obtained from the

overall carbon balance, i.e. the difference between the amount of consumed DEE and the sum of

quantified products, as shown in Figure 7.
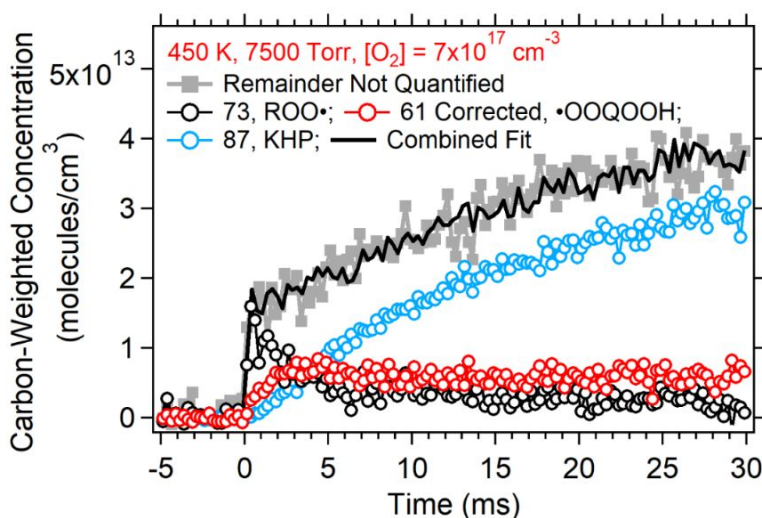


**Figure 7.** Time dependent carbon-weighted total concentration of unquantified products (filled squares), obtained from the difference between DEE consumption and the total concentration of products, quantified from references, at 450 K and 7500 Torr. The solid black line is a fit to a weighted sum of the time-dependent signals for ROO• (from $m/z$ 73, black circles), •OOQOOH (corrected $m/z$ 61, red circles), and KHP ($m/z$ 87, blue circles).

At 450 K and 7500 Torr, the time traces of ROO•, •OOQOOH, and KHP are sufficiently

distinct to enable the remaining carbon-weighted concentration to be accurately deconvolved into

the individual contributions of these intermediates. Because ROO• is produced almost

instantaneously, it is solely responsible for the missing carbon concentration immediately after $t =$

0 ms. Thus, the ROO• time trace (from $m/z$ 73) can be scaled to match the carbon-weighted

concentration of unquantified species at t = ~0 ms. The remaining missing concentration can then

be fit to a unique combination of the •OOQOOH (*m/z* 61, corrected for KHP) and KHP (*m/z* 87) time traces. As Figure 7 shows, the weighted sum of ROO•, •OOQOOH, and KHP time traces reproduces the total concentration of remaining unquantified species very well.

To obtain unique and reliable fits of these reactive intermediates from carbon balance, they must be produced with distinct formation/decay timescales and in comparable abundances. This requirement is fulfilled at 450 K, but not at higher or lower T. For example, at 400 K (Figure S14), the •OOQOOH and KHP concentrations are much smaller than that of ROO•, whereas at 500 – 600 K the formation of all 3 intermediates is quite fast and not easily distinguishable. Thus, T = 450 K is ideal for quantifying the time-resolved concentrations of ROO•, •OOQOOH, and KHP – key intermediates, for which authentic reference samples cannot be obtained.

**Absolute photoionization cross-sections.** The quantification of ROO•, •OOQOOH, and KHP enables their PI cross-sections, $\sigma_x$, to be determined from equation (1), using the measured PI spectra and time-integrated concentrations, $N_x$. These partial cross-sections are shown in Figure 8 for the *m/z* 73 DI channel of ROO•, the *m/z* 105 and 61 DI channels of •OOQOOH, and the parent cation (*m/z* 120) and the *m/z* 61 and 87 DI channels of KHP.

The PI cross-section for the DI fragment of ROO• at *m/z* 73 is shown in Figure 8(a). In addition to the measurement at 450 K and 7500 Torr, this cross-section was determined from five other experiments, with all results in good agreement. In all cases, ROO• was the only contribution to the missing carbon balance immediately after photolysis, which allowed its concentration to be reliably determined. Four of these measurements were performed at 400 K, 7300 Torr, and [O$_2$] = $(1.7 – 70) \times 10^{17}$ cm$^{-3}$. The last measurement was performed at 450 K, 50 Torr, and [O$_2$] = $2.5 \times 10^{17}$ cm$^{-3}$ using an established low-pressure MPIMS instrument,[24] which uses a different reactor and mass spectrometer design and has a different mass-dependent sensitivity bias. Furthermore, at 50

Torr the second $O_2$ addition reactions are diminished in importance (and •QOOH decomposition products enhanced), compared to the high-pressure experiments. Therefore, the 50 Torr measurement is an important independent confirmation of our high-pressure results of the ROO• ionization cross-section under substantially different conditions. The PI spectrum for the *m/z* 73 DI channel of ROO• in Figure 8 is the average of the six measurements (shown individually in Figure S15), with error bars equal to one standard deviation. The cross-section rises gradually from an onset at ~9.5 eV (~0.5 eV below the calculated VIE of ROO•) to reach ~8 Mb at 11 eV. Although R• (which has a parent cation at *m/z* 73) has an AIE of 6.2 eV (according to our calculations), we expect it to react with $O_2$ to form ROO• with a rate coefficient of ~$10^7$ $s^{-1}$ in our experiments and therefore not accumulate to any extent. Rather, the onset of *m/z* 73 ions below the calculated VIE of ROO• is likely due to the projection of the neutral wavefunction (which has amplitude over a range of R-OO bond lengths) onto a cation state that is repulsive along the R–OO coordinate. A cation ground electronic state that is unbound with respect to R–OO was previously calculated for ethyl peroxy and suggested generally for larger alkyl peroxy radicals.[52]

The absolute PI cross-section of •OOQOOH into the *m/z* 61 and 105 DI channels is shown in Figure 8(b). The *m/z* 61 channel has a cross-section of ~9 Mb at 11 eV, seven times higher than that of the *m/z* 105 channel. However, the *m/z* 61 channel has somewhat higher scatter in the data points because it had to be deconvolved from the KHP DI contribution at the same mass. According to Figures 4 and S9, the *m/z* 61 and 105 channels result from barrierless bond scissions of the unbound parent cation and lie ~1.3 eV and ~2.4 eV, respectively, lower in energy than the calculated VIE of •OOQOOH, ~10.1 eV. Both fragment ions have apparent onsets at ~9.7 eV, which is consistent with the calculated PES in Figure S9. The onsets are ~0.4 eV below the calculated VIE, similar to the onset of the PI spectrum of ROO•.
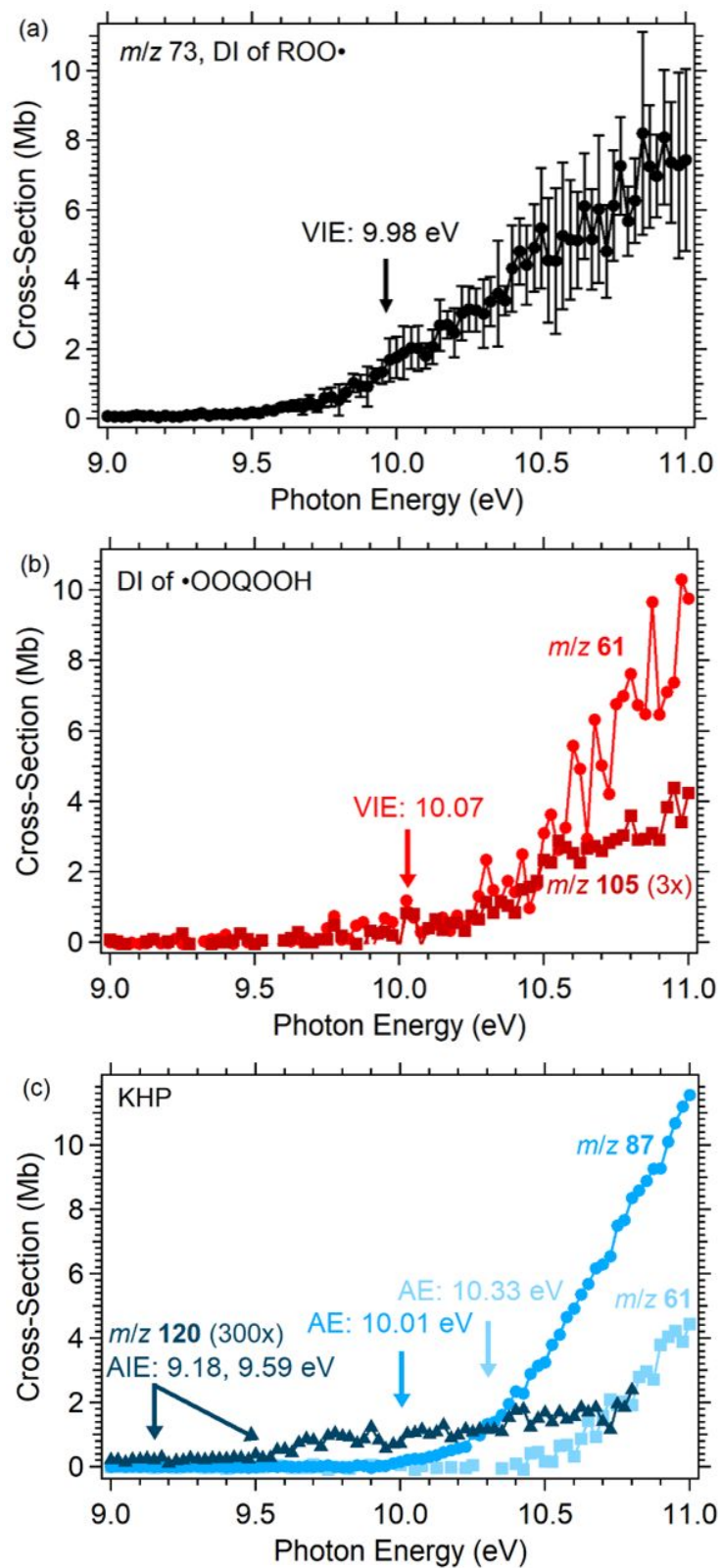
**Figure 8.** PI cross-sections for (a) ROO• into the *m/z* 73 channel, (b) •OOQOOH into the *m/z* 61 and 105 channels, and (c) KHP into the *m/z* 120, 61 and 87 channels.

The experimentally determined PI cross-section for KHP is presented in Figure 8(c). It is dominated by the DI fragments at *m/z* 61 and 87. Although our calculations indicate that the KHP parent cation (*m/z* 120) is stable, in most of our experiments we were unable to detect it, indicating that it is formed with extremely low yield. We were able to measure its PI spectrum and time trace at 500 K and 7300 Torr by employing large $O_2$ ($8\times10^{18}$ cm$^{-3}$), initial Cl atom (~$2\times10^{14}$ cm$^{-3}$), and DEE ($2\times10^{15}$ cm$^{-3}$) concentrations and extensive averaging as demonstrated in Figure S16. At these conditions significant radical recycling occurs such that reaction timescales and product branching are quite different from our baseline experiments; in addition, reaction pathways besides those shown in Scheme 2 may play a role. As a result, independent quantification of KHP from C atom balance and determination of its absolute PI cross-section is not feasible. The measured PI spectrum for the *m/z* 87 ions obtained with large $O_2$, Cl, and DEE concentrations differs from that in the baseline experiments due to new reaction products, as discussed in the Supplementary Information. However, the *m/z* 61 PI spectrum matches that of the baseline conditions well, and therefore the PI cross-section for the KHP parent cation at *m/z* 120 can be determined by referencing it to the DI peak at *m/z* 61. The resulting PI cross-section for the KHP cation at *m/z* 120 is included in Figure 8(c). This cross-section does not exceed ~0.006 Mb in the photon energy range measured, explaining the difficulty in observing the *m/z* 120 ion at the baseline conditions. The PI spectrum of the parent cation has a similar shape to that measured for the KHP cation of DME[50] and has an ionization onset at 9.5 eV, which is within the expected AIE range based on the calculated AIEs of the two KHP conformers considered here. Just as for DME, a broad distribution of KHP conformers, which is not explored here, may contribute to the observed ionization onset. The appearance energies of the *m/z* 87 and 61 DI fragment ions are ~10 eV and ~10.3 eV, respectively, in agreement with the calculated energy of the *m/z* 87 channel (~9.8 – 10 eV) and the

25

barrier to the *m/z* 61 channel (~10.1 – 10.3 eV).

The uncertainty in the partial PI cross-sections of ROO•, •OOQOOH, and KHP in Figure 8 arises mainly from the uncertainties in the cross-section of the reference compound (DEE, ~20% error), in the total missing carbon atom balance, and in the fitting used to deconvolve the time-dependent contribution of each intermediate. The second term depends in turn on the errors in the reference PI cross-sections of the quantified reaction products and the error in the correction for the mass-dependent detection efficiency. At 450 K and 7500 Torr, the contribution of all quantified products, excluding ROO•, •OOQOOH, and KHP, is only ~0.25 of the total carbon balance. Assuming that the reported errors (~20%) in each product reference cross-section are independent, the impact of their uncertainty on the much larger fraction (~0.75) of unquantified species is ± 7%. The uncertainty in the fits used to deconvolve the missing carbon balance into individual time traces gives errors of 10%, 9%, and 2.7% in the contributions of ROO•, •OOQOOH, and KHP, respectively. When all these uncertainties are propagated into the partial PI cross-sections, errors of ± ~22% are obtained for all three intermediates. However, the standard deviation of the six independent measurements of ROO• is somewhat larger, ± 35% (Figure 8(a)). This larger uncertainty better represents all systematic and statistical errors in our experiments, and therefore we propose that our measurements of the ROO•, •OOQOOH, and KHP cross-sections all have uncertainties of ± 35% (1σ).

It should be noted that ionization onsets of the KHP DI peaks shift to lower energies at lower reactor pressures. For *m/z* 87 this shift is ~0.08 and 0.15 eV (relative to the onset at 7500 Torr) when using reactor pressures of 3750 and 1500 Torr, respectively. In contrast, the PI spectra of *m/z* 73 (ROO•), 105 (•OOQOOH), or any other products do not exhibit pressure-dependent shifts, which rules out erroneous calibration of the ionizing photon energy. Nor is there evidence

for other DEE oxidation products with possible daughter ions at *m/z* 61 and 87 that could explain

the systematic shift to lower onsets with decreasing pressure. Rather, we conclude that the shift in

the onset is caused by changes in the local temperature of the ionized KHP. Photoionization in our

apparatus occurs inside a free-jet sampling expansion from the reactor into vacuum, such that

higher terminal Mach numbers and colder temperatures will be produced in the expansion from

higher pressure.[53] This may change the internal energy content of KHP or alter the conformer

distribution. Colder species are expected to require more energy to fragment, which is consistent

with the higher onsets we observe for the *m/z* 61 and 87 PI spectra at higher reactor pressures.

Alternatively, changes in the conformer distribution could also explain the shift. Of the two KHP

conformers considered here, the lowest-energy H-bonded conformer should be favored by higher-

pressure, colder expansions and should also have higher appearance energies for its DI fragments,

in agreement with the observed trend. This effect warrants further exploration that is outside the

scope of the current paper; however, we take the apparent pressure-dependence of the PI cross-

section into account for KHP quantification, as described below.

**Quantification using photoionization cross-sections.** At temperatures above 450 K the

rise times of ROO•, •OOQOOH, and KHP are no longer clearly distinct, and these intermediates

cannot be quantified by deconvolving their time-dependent contributions to the carbon balance.

However, their partial PI cross-sections determined at 450 K can be used to quantify these

intermediates using equation (1), as demonstrated in Figure 9 for 550 K and 7500 Torr.

The measured PI spectra of ROO• (*m/z* 73), •OOQOOH (*m/z* 105), and KHP (*m/z* 87) are

fit with the absolute PI cross-sections from Figure 8 to obtain scaling coefficients for equation (1).

Figure 9(b) shows the resulting time-dependent concentrations of ROO•, •OOQOOH, and KHP

from this quantification. Although the ROO• signal still rises more rapidly than the •OOQOOH

and KHP signals, all three intermediates reach their peak concentrations by $t = 2$ ms. The C atom balance, expressed as percent of DEE consumed, is ~100% at all kinetic times, indicating that all DEE oxidation products are accounted for by including ROO•, •OOQOOH, and KHP.
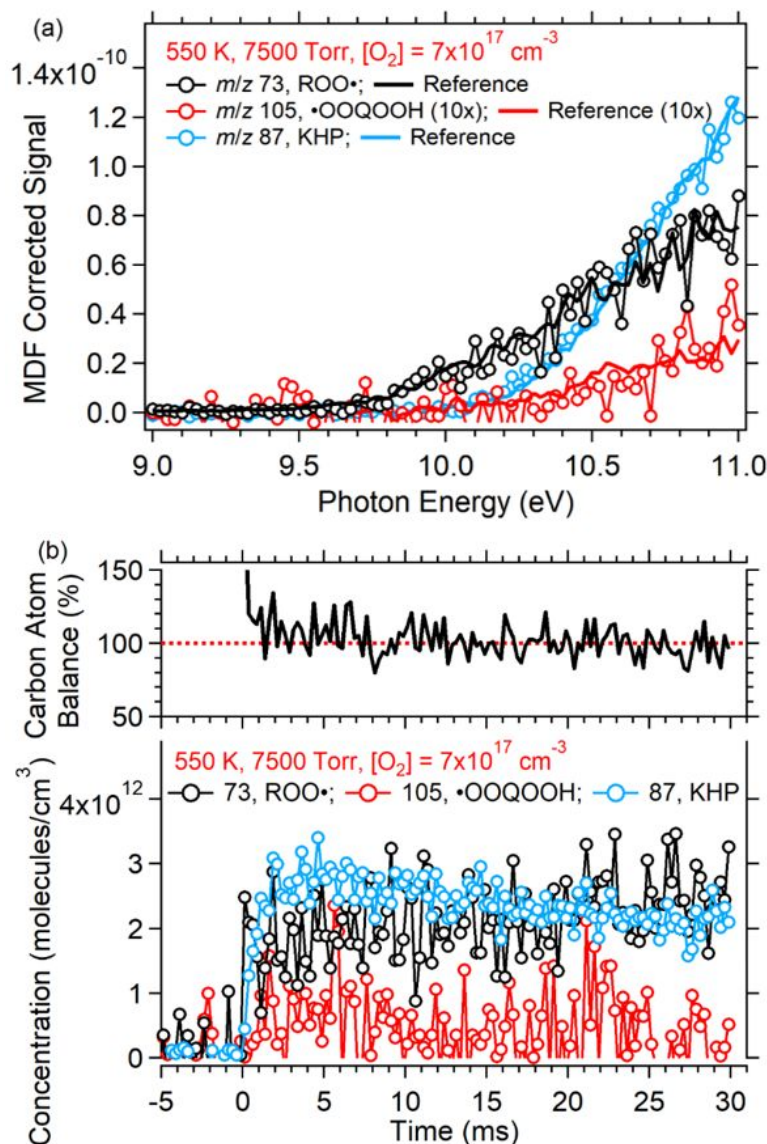


**Figure 9.** (a) PI spectra for the DI fragments of ROO• (*m/z* 73), •OOQOOH (*m/z* 105), and KHP (*m/z* 87) at 550 K and 7500 Torr. These PI spectra are fit with reference PI cross-sections (solid lines) from Figure 8 for quantification. (b) Time dependent concentration profiles (symbols) for ROO• (black), •OOQOOH (red), and KHP (blue), together with the resulting carbon atom balance (black line).

We repeated the time-resolved quantification analysis at other conditions, listed in Table

S1, ranging over T = 450 – 600 K, P = 1500 – 7500 Torr, and $[O_2] = (1.7 – 70) \times 10^{17}$ cm$^{-3}$. In all cases the total carbon atom balance was fulfilled well, with relatively constant deviations over $t =$ 0 – 30 ms ranging between 0 and 35%, as shown in Figures S18– S20. At P = 1500 and 3750 Torr the KHP cross-section into the $m/z$ 87 DI channel was shifted in energy as described above, and the additional uncertainty from this shift was considered $via$ two limiting-case treatments of the absolute PI cross-section. In one case, we simply shifted the reference $m/z$ 87 cross-section of Figure 8 to lower energy, thus increasing the area under the PI spectrum in our VUV photon energy range. In the second case, we shifted the PI spectrum and scaled it to keep the integrated PI cross-section the same. These scenarios provide reasonable upper and lower bounds to the KHP concentration, as demonstrated in Figure S21. The lower- and upper-bound KHP concentration-time profiles result in overall carbon atom imbalances of ~17% and 27%, respectively, which are still within the range observed for other conditions (Figures S18 – S20).

In summary, the errors in the overall carbon balance are typically near or below ~20%, but at times are as high as ± 35%. This is comparable to the uncertainties of ± 20% in the mole fractions of species, quantified via reference PI cross-sections, measured directly from samples of authentic standard compounds in previous MPIMS experiments.[31, 33] In fact, a part of the total error in the carbon balance may be due to errors in the concentrations of products determined from existing reference PI cross-sections. Therefore, the present measurements demonstrate that we can now quantify the key ephemeral intermediates in DEE oxidation – ROO•, •OOQOOH, and KHP – with accuracy approaching that of stable, commercially available end products. Our conclusions are predicated on the assumption of isomeric purity of α-ROO•, α,α'-•OOQOOH, and α,α'-KHP. Ongoing work in our group is exploring the validity of this assumption with help from quantum chemistry-based kinetic modeling.

**Trends with varying temperature, pressure, and O$_2$ concentration.** Our results permit an initial survey of the effects of temperature, pressure, and O$_2$ dependence on the mechanism of low-temperature DEE oxidation. A full-scale study aimed at validating the sub-mechanism of initiation reactions in DEE autoignition is underway and will be reported in a future publication. Average yields of acetaldehyde, ROO•, •OOQOOH, KHP, and acetic acid (defined as the fraction of total products, averaged over $t = 0 - 30$ ms) as a function of temperature at 7500 Torr and [O$_2$] $= 7 \times 10^{17}$ cm$^{-3}$ are shown in Figure 10(a). The main trends we observe are a decrease in the yields of •OOQOOH and KHP and an increase in the yields of acetaldehyde and ROO• with increasing temperature. These trends can be explained by an increase in thermal decomposition of •QOOH at higher T, leading to a decrease in the second O$_2$ addition. Because •QOOH decomposition results in radical chain propagating (rather than branching) pathways, its increasing dominance over second O$_2$ addition was used by Tran *et al.* to explain the decrease in DEE reactivity in the first NTC zone, $500 - 600$ K.[14] Acetic acid exhibits complex behavior as a function of temperature, which might arise from competition among KHP decomposition pathways.

Figure 10(b) shows the pressure dependence at 500 K for the average yields of ROO•, •OOQOOH, KHP, acetaldehyde, and acetic acid. The yields of KHP and •OOQOOH increase, whereas those of acetic acid and acetaldehyde decrease with increasing pressure, possibly due to three effects. Stabilization of •QOOH may decrease the yield of acetaldehyde formed by chemically activated •QOOH. Stabilization of •OOQOOH should accelerate the approach to the •QOOH + O$_2$ ↔ •OOQOOH equilibrium, also reducing the prompt yield of acetaldehyde from •QOOH. The decrease in acetic acid as a function of pressure may suggest that it is also produced at least in part from chemically activated KHP. Pressure does not affect the average yield of ROO•, which can be explained by the reaction of R• with O$_2$ already being in the high-pressure limit.
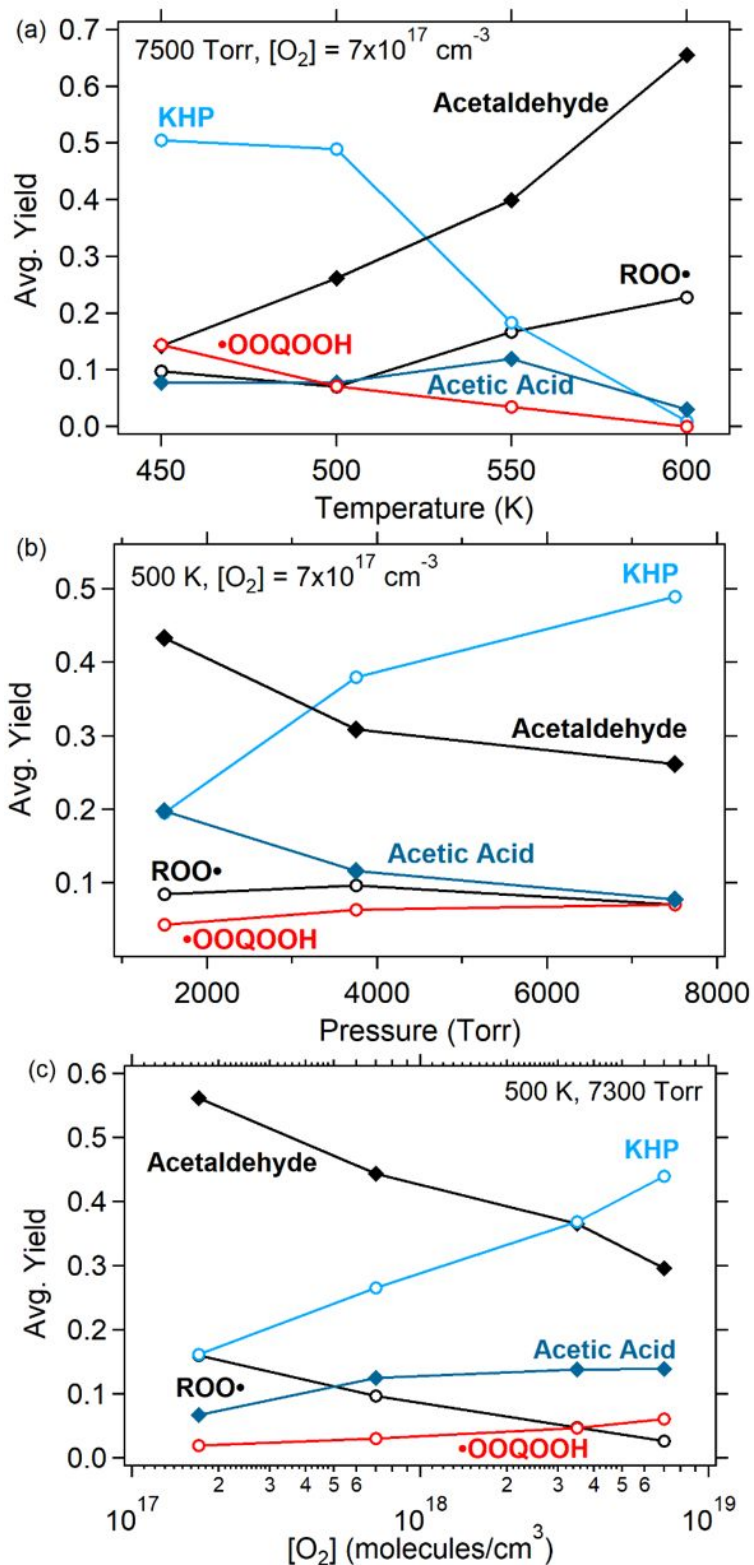
**Figure 10.** (a) Average yield of ROO•, •OOQOOH, KHP, acetaldehyde, and acetic acid as a function of (a) temperature at 7500 Torr and $[O_2] = 7\times10^{17}$ cm$^{-3}$, (b) pressure at 500 K and $[O_2] = 7\times10^{17}$ cm$^{-3}$, and (c) $O_2$ concentration at 500 K and 7300 Torr.

The effect of varying $O_2$ concentration on the average yields at 7300 Torr and 500 K is shown in Figure 10(c). Increasing $[O_2]$ results in increasing yields of •OOQOOH, KHP, and acetic acid while decreasing those of acetaldehyde and ROO•. These trends are easily explained by higher $O_2$ levels favoring the second $O_2$ addition pathways at the expense of the first $O_2$ addition channels (Scheme 2). Quantification of ROO•, •OOQOOH, and KHP at these and other experimental conditions will be complemented by kinetics modeling in a future publication. The trends from these studies should reveal important information regarding the competition between radical chain branching and propagating pathways as a function of various conditions and lead to a detailed understanding of the low-temperature oxidation of DEE.

**Conclusions**

We employed synchrotron-based photoionization mass spectrometry to directly observe three critical intermediates (ROO•, •OOQOOH, and KHP) in the oxidation of a prototypical linear ether, diethyl ether. The mass peaks of DI fragments were assigned with the aid of theory, by comparing calculated energetics with experimental onsets, and with the help of the distinct formation timescales exhibited by ROO•, •OOQOOH, and KHP at 450 K and 7500 Torr. This separation of timescales enabled the determination of absolute concentrations (with typical uncertainties of ±35% or less) of ROO•, •OOQOOH, and KHP directly from experiment, using the total carbon balance. This quantification in turn allowed us to obtain directly from experiment the absolute PI cross-sections of the reactive chemical intermediates ROO•, •OOQOOH, and KHP. Such PI cross-section measurements are not possible by conventional means (i.e. using authentic standard samples) for short-lived, reactive species.

The PI cross-sections determined in this work were successfully applied to quantify ROO•, •OOQOOH, and KHP at a range of experimental temperatures, pressures, and $O_2$ concentrations.

The results illuminate trends in the competition between second $O_2$ addition reactions (responsible for radical chain branching), and decomposition pathways (responsible for radical chain propagation or inhibition) in low-temperature DEE oxidation. More extensive quantification studies over a greater range of conditions, coupled with kinetics modeling, are currently underway and should provide a detailed picture of the reactivity of DEE and its low-temperature oxidation mechanism. More broadly, the methodology presented here can be used to explore the fundamental photophysics of elusive radicals and unstable closed-shell compounds, as well as directly probe and quantify these intermediates in complex reaction networks.

**Electronic Supplementary Information**

Reference PI cross-sections measured in this work; details of product quantification; analysis of PI spectra; calculated cation PESs for ROO•, •OOQOOH, and KHP, and DI fragment assignments.

**Acknowledgements**

## References

1. M. Ehn, J. A. Thornton, E. Kleist, M. Sipila, H. Junninen, I. Pullinen, M. Springer, F. Rubach, R. Tillmann, B. Lee, F. Lopez-Hilfiker, S. Andres, I. H. Acir, M. Rissanen, T. Jokinen, S. Schobesberger, J. Kangasluoma, J. Kontkanen, T. Nieminen, T. Kurten, L. B. Nielsen, S. Jorgensen, H. G. Kjaergaard, M. Canagaratna, M. D. Maso, T. Berndt, T. Petaja, A. Wahner, V. M. Kerminen, M. Kulmala, D. R. Worsnop, J. Wildt and T. F. Mentel, *Nature*, 2014, **506**, 476-479.
2. J. Zádor, C. A. Taatjes and R. X. Fernandes, *Prog. Energy Combust. Sci.*, 2011, **37**, 371-421.
3. M. Krishnamoorthi, R. Malayalamurthi, Z. He and S. Kandasamy, *Renew. Sustain. Energy Rev.*, 2019, **116**, 109404(109401)-109404(109453).
4. J. E. Dec, *Proc. Combust. Inst.*, 2009, **32**, 2727-2742.
5. M. Yao, Z. Zheng and H. Liu, *Prog. Energy Combust. Sci.*, 2009, **35**, 398-437.
6. D. C. Rakopoulos, C. D. Rakopoulos, E. G. Giakoumis and A. M. Dimaratos, *Energy*, 2012, **43**, 214-224.
7. A. Paul, P. K. Bose, R. Panua and D. Debroy, *J. Energy Inst.*, 2015, **88**, 1-10.
8. F. Gillespie, W. K. Metcalfe, P. Dirrenberger, O. Herbinet, P. A. Glaude, F. Battin-Leclerc and H. J. Curran, *Energy*, 2012, **43**, 140-145.
9. J. Hashimoto, K. Tanoue, N. Taide and Y. Nouno, *Proc. Combust. Inst.*, 2015, **35**, 973-980.
10. L.-S. Tran, J. Pieper, H.-H. Carstensen, H. Zhao, I. Graf, Y. Ju, F. Qi and K. Kohse-Höinghaus, *Proc. Combust. Inst.*, 2017, **36**, 1165-1173.
11. N. Vin, O. Herbinet and F. Battin-Leclerc, *J. Anal. Appl. Pyrolysis*, 2016, **121**, 173-176.
12. M. Werler, L. R. Cancino, R. Schiessl, U. Maas, C. Schulz and M. Fikri, *Proc. Combust. Inst.*, 2015, **35**, 259-266.
13. K. Yasunaga, F. Gillespie, J. M. Simmie, H. J. Curran, Y. Kuraguchi, H. Hoshikawa, M. Yamane and Y. Hidaka, *J. Phys. Chem. A*, 2010, **114**, 9098-9109.
14. L.-S. Tran, O. Herbinet, Y. Li, J. Wullenkord, M. Zeng, E. Bräuer, F. Qi, K. Kohse-Höinghaus and F. Battin-Leclerc, *Proc. Combust. Inst.*, 2019, **37**, 511-519.
15. F. Battin-Leclerc, O. Herbinet, P. A. Glaude, R. Fournet, Z. Zhou, L. Deng, H. Guo, M. Xie and F. Qi, *Angew. Chem., Int. Ed.*, 2010, **49**, 3169-3172.
16. J. D. Savee, E. Papajak, B. Rotavera, H. Huang, A. J. Eskola, O. Welz, L. Sheps, C. A. Taatjes, J. Zádor and D. L. Osborn, *Science*, 2015, **347**, 643-646.
17. J. Zador, H. Huang, O. Welz, J. Zetterberg, D. L. Osborn and C. A. Taatjes, *Phys. Chem. Chem. Phys.*, 2013, **15**, 10753-10760.
18. O. Kostko, B. Bandyopadhyay and M. Ahmed, *Annu. Rev. Phys. Chem.*, 2016, **67**, 19-40.
19. F. Qi, *Proc. Combust. Inst.*, 2013, **34**, 33-63.
20. T. A. Cool, A. McIlroy, F. Qi, P. R. Westmoreland, L. Poisson, D. S. Peterka and M. Ahmed, *Rev. Sci. Instrum.*, 2005, **76**, 094102.
21. P. T. Lynch, T. P. Troy, M. Ahmed and R. S. Tranter, *Anal. Chem.*, 2015, **87**, 2345-2352.
22. C. A. Taatjes, N. Hansen, D. L. Osborn, K. Kohse-Hoinghaus, T. A. Cool and P. R. Westmoreland, *Phys. Chem. Chem. Phys.*, 2008, **10**, 20-34.
23. N. Hansen, T. A. Cool, P. R. Westmoreland and K. Kohse-Höinghaus, *Prog. Energy Combust. Sci.*, 2009, **35**, 168-191.
24. D. L. Osborn, P. Zou, H. Johnsen, C. C. Hayden, C. A. Taatjes, V. D. Knyazev, S. W. North, D. S. Peterka, M. Ahmed and S. R. Leone, *Rev. Sci. Instrum.*, 2008, **79**, 104103.

25.  L. Sheps, I. Antonov and K. Au, *J. Phys. Chem. A*, 2019, **123**, 10804-10814.
26.  O. Welz, J. Zador, J. D. Savee, M. Y. Ng, G. Meloni, R. X. Fernandes, L. Sheps, B. A. Simmons, T. S. Lee, D. L. Osborn and C. A. Taatjes, *Phys. Chem. Chem. Phys.*, 2012, **14**, 3112-3127.
27.  O. Welz, J. Zador, J. D. Savee, L. Sheps, D. L. Osborn and C. A. Taatjes, *J. Phys. Chem. A*, 2013, **117**, 11983-12001.
28.  A. J. Eskola, O. Welz, J. D. Savee, D. L. Osborn and C. A. Taatjes, *J. Phys. Chem. A*, 2013, **117**, 12216-12235.
29.  O. Welz, M. P. Burke, I. O. Antonov, C. F. Goldsmith, J. D. Savee, D. L. Osborn, C. A. Taatjes, S. J. Klippenstein and L. Sheps, *J. Phys. Chem. A*, 2015, **119**, 7116-7129.
30.  A. J. Eskola, O. Welz, J. Zádor, I. O. Antonov, L. Sheps, J. D. Savee, D. L. Osborn and C. A. Taatjes, *Proc. Combust. Inst.*, 2015, **35**, 291-298.
31.  I. O. Antonov, J. Zador, B. Rotavera, E. Papajak, D. L. Osborn, C. A. Taatjes and L. Sheps, *J. Phys. Chem. A*, 2016, **120**, 6582-6595.
32.  A. J. Eskola, I. O. Antonov, L. Sheps, J. D. Savee, D. L. Osborn and C. A. Taatjes, *Phys. Chem. Chem. Phys.*, 2017, **19**, 13731-13745.
33.  B. Rotavera, J. D. Savee, I. O. Antonov, R. L. Caravan, L. Sheps, D. L. Osborn, J. Zádor and C. A. Taatjes, *Proc. Combust. Inst.*, 2017, **36**, 597-606.
34.  J. C. Davis, A. L. Koritzke, R. L. Caravan, I. O. Antonov, M. G. Christianson, A. C. Doner, D. L. Osborn, L. Sheps, C. A. Taatjes and B. Rotavera, *J. Phys. Chem. A*, 2019, **123**, 3634-3646.
35.  J. D. Savee, S. Soorkia, O. Welz, T. M. Selby, C. A. Taatjes and D. L. Osborn, *J. Chem. Phys.*, 2012, **136**, 134307.
36.  B. Ghosh, D. K. Papanastasiou and J. B. Burkholder, *J. Chem. Phys.*, 2012, **137**, 164315.
37.  M. J. Frisch, G. W. Trucks, H. B. Schlegel, G. E. Scuseria, M. A. Robb, J. R. Cheeseman, G. Scalmani, V. Barone, G. A. Petersson, H. Nakatsuji, X. Li, M. Caricato, A. V. Marenich, J. Bloino, B. G. Janesko, R. Gomperts, B. Mennucci, H. P. Hratchian, J. V. Ortiz, A. F. Izmaylov, J. L. Sonnenberg, Williams, F. Ding, F. Lipparini, F. Egidi, J. Goings, B. Peng, A. Petrone, T. Henderson, D. Ranasinghe, V. G. Zakrzewski, J. Gao, N. Rega, G. Zheng, W. Liang, M. Hada, M. Ehara, K. Toyota, R. Fukuda, J. Hasegawa, M. Ishida, T. Nakajima, Y. Honda, O. Kitao, H. Nakai, T. Vreven, K. Throssell, J. A. Montgomery Jr., J. E. Peralta, F. Ogliaro, M. J. Bearpark, J. J. Heyd, E. N. Brothers, K. N. Kudin, V. N. Staroverov, T. A. Keith, R. Kobayashi, J. Normand, K. Raghavachari, A. P. Rendell, J. C. Burant, S. S. Iyengar, J. Tomasi, M. Cossi, J. M. Millam, M. Klene, C. Adamo, R. Cammi, J. W. Ochterski, R. L. Martin, K. Morokuma, O. Farkas, J. B. Foresman and D. J. Fox, Wallingford, CT2016.
38.  J. A. Montgomery, Jr., M. J. Frisch, J. W. Ochterski and G. A. Petersson, *J. Chem. Phys.*, 2000, **112**, 6532-6542.
39.  T. A. Cool, K. Nakajima, T. A. Mostefaoui, F. Qi, A. McIlroy, P. R. Westmoreland, M. E. Law, L. Poisson, D. S. Peterka and M. Ahmed, *J. Chem. Phys.*, 2003, **119**, 8356-8365.
40.  T. A. Cool, J. Wang, K. Nakajima, C. A. Taatjes and A. McLlroy, *Int. J. Mass spectrom.*, 2005, **247**, 18-27.
41.  L. G. Dodson, L. Shen, J. D. Savee, N. C. Eddingsaas, O. Welz, C. A. Taatjes, D. L. Osborn, S. P. Sander and M. Okumura, *J. Phys. Chem. A*, 2015, **119**, 1279-1291.
42.  B. Yang, J. Wang, T. A. Cool, N. Hansen, S. Skeen and D. L. Osborn, *Int. J. Mass spectrom.*, 2012, **309**, 118-128.

43.    A. C. Doner, M. M. Davis, A. L. Koritzke, M. G. Christianson, J. M. Turney, H. F. I. Schaefer, L. Sheps, D. L. Osborn, C. A. Taatjes and B. Rotavera, *submitted to Int. J. Chem. Kinet.*, 2020.
44.    O. Herbinet, B. Husson, Z. Serinyel, M. Cord, V. Warth, R. Fournet, P. A. Glaude, B. Sirjean, F. Battin-Leclerc, Z. Wang, M. Xie, Z. Cheng and F. Qi, *Combust. Flame*, 2012, **159**, 3455-3471.
45.    Y. Sakai, H. Ando, H. K. Chakravarty, H. Pitsch and R. X. Fernandes, *Proc. Combust. Inst.*, 2015, **35**, 161-169.
46.    Y. Sakai, J. Herzler, M. Werler, C. Schulz and M. Fikri, *Proc. Combust. Inst.*, 2017, **36**, 195-202.
47.    A. D. Danilack, S. J. Klippenstein and C. F. Goldsmith, *Proc. Combust. Inst.*, 2020.
48.    B. B. Darwent and U. S. D. Commerce, *Bond Dissociation Energies in Simple Molecules*, U.S. National Bureau of Standards1970.
49.    J. M. Simmie, *J. Phys. Chem. A*, 2012, **116**, 4528-4538.
50.    K. Moshammer, A. W. Jasper, D. M. Popolan-Vaida, A. Lucassen, P. Dievart, H. Selim, A. J. Eskola, C. A. Taatjes, S. R. Leone, S. M. Sarathy, Y. Ju, P. Dagaut, K. Kohse-Hoinghaus and N. Hansen, *J. Phys. Chem. A*, 2015, **119**, 7361-7374.
51.    K. Voronova, C. M. Mozaffari Easter, K. G. Torma, A. Bodi, P. Hemberger and B. Sztaray, *Phys. Chem. Chem. Phys.*, 2016, **18**, 25161-25168.
52.    G. Meloni, P. Zou, S. J. Klippenstein, M. Ahmed, S. R. Leone, C. A. Taatjes and D. L. Osborn, *J. Am. Chem. Soc.*, 2006, **128**, 13559-13567.
53.    M. Morse, in *Experimental Methods in The Physical Sciences*1996, vol. 29, ch. 2, pp. 21-47.